Y. Wang, F. Topputo
Indirect Optimization of Power-Limited Asteroid Rendezvous Trajectories
Journal of Guidance Control and Dynamics, In press - Published online 14/02/2022
doi:10.2514/1.G006179

Indirect Optimization of Power-Limited Asteroid Rendezvous Trajectories

Yang Wang * and Francesco Topputo †
Politecnico di Milano, Via La Masa 34, Milan, Italy, 20156

I. Introduction

Owing to the higher specific impulse compared to chemical propulsion, low-thrust solar electric propulsion (SEP) enables various types of space missions with a relatively smaller amount of thrust [1]. Yet, the SEP-driven trajectory optimization is challenging since the engine operates during a significant fraction of the flight, and the thrust level depends upon power availability [1].

Numerical methods that solve a nonlinear optimal control problem (NOCP) are mainly categorized as direct methods and indirect methods [2]. Direct methods convert an infinite-dimensional NOCP into a finite-dimensional nonlinear programming problem by transcription and collocation [3]. Direct methods can handle path and boundary constraints easily, but many parameters and high-order integrators are usually required to obtain an accurate solution [4]. Indirect methods transform a NOCP into a two-point boundary value problem (TPBVP) or a multi-point boundary value problem (MPBVP) if interior-point constraints are involved [3, 5]. Then, the NOCP is solved as a zero-finding problem, with the solution satisfying first-order optimality conditions [3]. However, guessing initial costate values is challenging due to the narrow convergence domain of zero-finding methods [2].

Incorporating an accurate SEP engine model into indirect optimization improves mass budget estimation. The electrical power to accelerate the propellant used by most SEP thrusters varies with heliocentric distance [6]. In turn, the thrust, propellant mass flow rate, and specific impulse vary as a function of the input power [6–8]. Due to technological constraints, the input power to the engine is limited, and the related bounded values are key thruster parameters [6–8]. That is, the spacecraft flies ballistically if insufficient power is provided [9], while the input power is capped when excess power is available [10]. Therefore, the convergence difficulty is exacerbated by dynamics discontinuities produced by power constraints [11]. Smoothing techniques have been employed in [11–13]. Power operation detection was developed in [14] to improve solution accuracy. In indirect optimization, the gradients of nonlinear constraints with respect to problem decision variables are critical for most zero-finding methods [15]. However, the effects of power constraints on the gradients and the optimal solution are still unexplored.

This Note analyzes this issue and further presents an efficient indirect method featuring analytic gradients for SEP-based trajectory optimization. First, the NOCP with scalar interior-point constraints is formulated. Analytical

*PhD candidate, Department of Aerospace Science and Technology; E-mail: yang.wang@polimi.it (Corresponding Author).
†Full professor, Department of Aerospace Science and Technology; E-mail: francesco.topputo@polimi.it. AIAA senior member.

multipliers related to interior-point constraints are obtained. This intermediate result is leveraged to tackle a MPBVP as a TPBVP. Second, the state transition matrix (STM), which provides sensitivities of states and costates at different time instants along a given trajectory [16], is employed to compute the gradients. The STM across costate and dynamics discontinuities produced by bang-bang control and power constraints is analyzed. Third, in order to ease the costate initialization, two continuation methods are used to approach a discontinuous control by a consecutive sequence of continuous controls: 1) energy- to fuel-optimal continuation, to mitigate the convergence difficulty associated to bang-bang control in the fuel-optimal problems, and 2) Hyperbolic Tangent Smoothing (HTS), to handle engine switch on/off related to power bounds. The advancement to the HTS in [17] consists of the capability to achieve the desired discontinuous solution. Finally, the flowchart in [18] is augmented by adding branches that address power constraints. Overall, a computational framework is set up by integrating analytic derivatives, continuation and switching detection into the augmented flowchart, so enabling the computation of accurate bang-bang solutions and their gradients.

Applications involve the case of M-ARGO, the Miniaturised Asteroid Remote Geophysical Observer [19]. M-ARGO is proposed as the first ESA stand-alone CubeSat mission to rendezvous with and characterize a near-Earth asteroid (NEA) [19]. The developed method has been applied successfully to perform a comprehensive target screening [20].

The Note is structured as follows. Sec. II presents the problem statement of power-limited low-thrust trajectory optimization. Sec. III describes initialization of guess solution. The STM is derived in Sec. IV. In Sec. V, the switching detection technique is presented and incorporated into an augmented flowchart. Sec. VI presents numerical simulations for asteroid rendezvous. Finally, Sec. VII reports concluding remarks.

II. Problem Statement

A. Mathematical Model

The heliocentric phase of an interplanetary orbit transfer problem is considered. The equations of motion are

$$\dot{\boldsymbol{x}} = \boldsymbol{f}(\boldsymbol{x}, u, \boldsymbol{\alpha}) \Rightarrow \begin{cases} \dot{\boldsymbol{r}} = \boldsymbol{v} \\ \dot{\boldsymbol{v}} = -\dfrac{\mu}{r^3}\boldsymbol{r} + u\dfrac{T_{\max}}{m}\boldsymbol{\alpha} \\ \dot{m} = -u\dfrac{T_{\max}}{I_{\mathrm{sp}}\, g_0} \end{cases} \tag{1}$$

where $\boldsymbol{r}$, $\boldsymbol{v}$, and m are the spacecraft position vector, velocity vector, and mass, respectively; $\boldsymbol{x} := [\boldsymbol{r}^\top, \boldsymbol{v}^\top, m]^\top$ is the state vector, $u \in [0, 1]$ is the thrust throttle factor and $\boldsymbol{\alpha}$ is the thrust direction unit vector; g_0 is the gravitational acceleration at sea level. Both the maximum thrust $T_{\max}$ and the specific impulse I_{sp} are assumed to vary with the engine input power P_{in}, i.e. , $T_{\max} = T_{\max}(P_{\mathrm{in}})$ and $I_{\mathrm{sp}} = I_{\mathrm{sp}}(P_{\mathrm{in}})$. It is assumed that $P_{\mathrm{in}} = P_{\mathrm{in}}(r)$ is a function of the spacecraft-Sun distance.

We define $S_p = S_p(r)$ as the power switching function used to detect the thruster operation logic (see Fig. 1):

$$\text{if } S_p(r) \geq P_{\max} \quad \text{then} \quad P_{\text{in}} = P_{\max},\ u \in [0,1] \tag{2}$$

$$\text{if } S_p(r) \in [P_{\min}, P_{\max}) \quad \text{then} \quad P_{\text{in}} = S_p(r),\ u \in [0,1] \tag{3}$$

$$\text{if } S_p(r) < P_{\min} \quad \text{then} \quad P_{\text{in}} = S_p(r),\ u = 0 \tag{4}$$

where $P_{\max}$ and $P_{\min}$ are upper and lower bounds of power input to the engine, respectively.

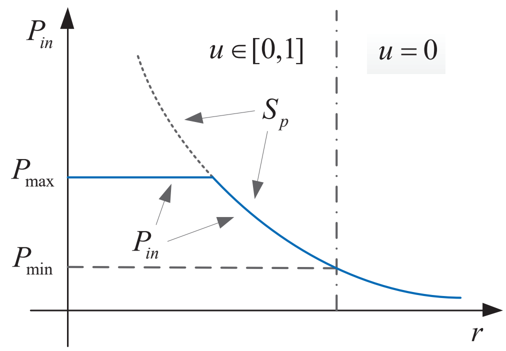

Fig. 1 Geometric relationship between P_{in} and S_p.

Remark 1 *In actual flight, the engine switches off when $S_p < P_{\min}$, so implying $P_{\text{in}} = 0$. However, to mimic a ballistic flight, we set $P_{\text{in}} = S_p$ and $u = 0$ for trajectory optimization purposes. Setting P_{in} to 0 creates discontinuity that artificially increases the complexity of the problem.*

B. Fuel-Optimal Problem

With t_i and t_f given, the fuel-optimal problem is to minimize

$$J_f = \int_{t_i}^{t_f} u \frac{T_{\max}}{I_{\text{sp}}\, g_0}\, \mathrm{d}t \tag{5}$$

under the following boundary conditions

$$\boldsymbol{r}(t_i) - \boldsymbol{r}_i = 0, \quad \boldsymbol{v}(t_i) - \boldsymbol{v}_i = 0, \quad m(t_i) - m_i = 0 \tag{6}$$

$$\boldsymbol{r}(t_f) - \boldsymbol{r}_t(t_f) = 0, \quad \boldsymbol{v}(t_f) - \boldsymbol{v}_t(t_f) = 0 \tag{7}$$

where $\boldsymbol{r}_t(t)$ are $\boldsymbol{v}_t(t)$ are the known time-dependent position and velocity vectors of the moving target body, respectively.

Since the optimal thrust throttle profile u^* is bang-bang, a smoothing technique is implemented to gradually enforce this discontinuity. The following objective function [21]

$$J_\varepsilon = \int_{t_i}^{t_f} \frac{T_{\max}}{I_{\mathrm{sp}}\, g_0} \left[u - \varepsilon u(1-u)\right] \mathrm{d}t \tag{8}$$

yields an energy-optimal problem for $\varepsilon = 1$ and a fuel-optimal problem for $\varepsilon = 0$. The idea is to solve an energy-optimal problem (with t_i, t_f given and the boundary conditions in Eqs. (6)-(7)) and to continue the solution manifold while gradually reducing ε, until the fuel-optimal problem is solved [18].

The Hamiltonian of the auxiliary problem is

$$H_\varepsilon = \boldsymbol{\lambda}_r \cdot \boldsymbol{v} + \boldsymbol{\lambda}_v \cdot \left(-\frac{\mu}{r^3}\boldsymbol{r} + u\frac{T_{\max}}{m}\boldsymbol{\alpha}\right) + \lambda_m \left(-u\frac{T_{\max}}{I_{\mathrm{sp}}\, g_0}\right) + \frac{T_{\max}}{I_{\mathrm{sp}}\, g_0}\left[u - \varepsilon u(1-u)\right] \tag{9}$$

where $\boldsymbol{\lambda} := [\boldsymbol{\lambda}_r^\top, \boldsymbol{\lambda}_v^\top, \lambda_m]^\top$ is the vector of Lagrange multipliers (costates) associated to $\boldsymbol{x}$. The optimal thrust direction is such that H is minimized at any time by virtue of the Pontryagin minimum principle (PMP) [22], i.e.,

$$\boldsymbol{\alpha}^* = -\frac{\boldsymbol{\lambda}_v}{\lambda_v} \tag{10}$$

where $\lambda_v = \|\boldsymbol{\lambda}_v\|_2$ is the Euclidean norm of $\boldsymbol{\lambda}_v$. Substituting Eq. (10) into Eq. (9) yields

$$H_\varepsilon = \boldsymbol{\lambda}_r \cdot \boldsymbol{v} - \frac{\mu}{r^3}\boldsymbol{r} \cdot \boldsymbol{\lambda}_v + \frac{T_{\max}}{I_{\mathrm{sp}}\, g_0} u \left(S_\varepsilon - \varepsilon + \varepsilon u\right) \tag{11}$$

where the throttle switching function S_ε is

$$S_\varepsilon = 1 - \lambda_m - \frac{I_{\mathrm{sp}}\, g_0}{m}\lambda_v \tag{12}$$

The optimal throttle factor u^* is determined by the PMP and the power availability, as

$$u^* = \begin{cases} 0 & S_\varepsilon > \varepsilon \quad \text{or} \quad S_p < P_{\min} \\ 1 & S_\varepsilon < -\varepsilon \quad \text{and} \quad S_p \geq P_{\min} \\ \dfrac{\varepsilon - S_\varepsilon}{2\varepsilon} & |S_\varepsilon| \leq \varepsilon \quad \text{and} \quad S_p \geq P_{\min} \end{cases} \tag{13}$$

Remark 2 *An interior-point constraint should be addressed to ensure that Eq.* (13) *satisfies necessary conditions of optimality; see Sec. II.D.*

The motion of the spacecraft can be determined by integrating the following state-costate dynamics

$$\dot{\boldsymbol{y}} = \boldsymbol{F}_{\varepsilon}(\boldsymbol{y}) \Rightarrow \begin{cases} \dot{\boldsymbol{x}} = \left(\dfrac{\partial H_{\varepsilon}}{\partial \boldsymbol{\lambda}}\right)^{\top} \\ \dot{\boldsymbol{\lambda}} = -\left(\dfrac{\partial H_{\varepsilon}}{\partial \boldsymbol{x}}\right)^{\top} \end{cases} \tag{14}$$

where $\boldsymbol{y} := [\boldsymbol{x}^{\top}, \boldsymbol{\lambda}^{\top}]^{\top}$. Note that Eq. (14), as well as Eq. (21), has two different expressions based on whether $P_{\text{in}} = P_{\max}$ or not. Since the terminal mass is free and the augmented terminal cost does not explicitly depend on the mass, there exists

$$\lambda_m(t_f) = 0 \tag{15}$$

C. Time-Optimal Problem

In a time-optimal problem, the spacecraft has to rendezvous with a moving target [14]. The terminal conditions are the same as in Eq. (7), but in this case t_f is free. The objective function is

$$J_t = \int_{t_i}^{t_f} 1 \, \mathrm{d}t \tag{16}$$

thus the Hamiltonian reads

$$H_t = \boldsymbol{\lambda}_r \cdot \boldsymbol{v} + \boldsymbol{\lambda}_v \cdot \left(-\frac{\mu}{r^3}\boldsymbol{r} + u\frac{T_{\max}}{m}\boldsymbol{\alpha}\right) - \lambda_m u \frac{T_{\max}}{I_{\text{sp}}\, g_0} + 1 \tag{17}$$

The optimal thrust direction $\boldsymbol{\alpha}^*$ is again given by Eq. (10), whereas the optimal throttle factor u^* is

$$u^* = \begin{cases} 0 & S_t > 0 \quad \text{or} \quad S_p < P_{\min} \\ 1 & S_t < 0 \quad \text{and} \quad S_p \geq P_{\min} \\ \in [0, 1] & S_t = 0 \quad \text{and} \quad S_p \geq P_{\min} \end{cases} \tag{18}$$

where the time-optimal throttle switching function is

$$S_t = -\lambda_v \frac{I_{\text{sp}}\, g_0}{m} - \lambda_m \tag{19}$$

The transversality condition at terminal time t_f is [14]

$$H_t(t_f) - \boldsymbol{\lambda}_r(t_f) \cdot \boldsymbol{v}_t(t_f) - \boldsymbol{\lambda}_v(t_f) \cdot \boldsymbol{a}_t(t_f) = 0 \tag{20}$$

where $\boldsymbol{a}_t$ is the acceleration of the target body.

The motion of the spacecraft can be determined by integrating the following state-costate dynamics

$$\dot{\boldsymbol{y}} = \boldsymbol{F}_t(\boldsymbol{y}) \Rightarrow \begin{cases} \dot{\boldsymbol{x}} = \left(\dfrac{\partial H_t}{\partial \boldsymbol{\lambda}}\right)^\top \\ \dot{\boldsymbol{\lambda}} = -\left(\dfrac{\partial H_t}{\partial \boldsymbol{x}}\right)^\top \end{cases} \tag{21}$$

D. Interior-Point Constraint

When $S_p < P_{\min}$ in Eq. (4), insufficient power is generated, and the engine switches off ($u = 0$). However, according to the PMP, this action may not be optimal since it is not related to the minimization of the Hamiltonian (Eqs. (11) and (17)). In order to satisfy the necessary conditions of optimality, this event should be treated as an interior-point constraint [22]. Suppose that S_p crosses $P_{\min}$ at t_s, the following conditions have to be satisfied [22]

$$H(t_s^-) = H(t_s^+) - \pi \frac{\partial S_p}{\partial t} \tag{22}$$

$$\boldsymbol{\lambda}_r^\top(t_s^-) = \boldsymbol{\lambda}_r^\top(t_s^+) + \pi \frac{\partial S_p}{\partial \boldsymbol{r}} \tag{23}$$

where t_s^- and t_s^+ are time instants before and after t_s, π is a scalar Lagrange multiplier, and $\partial S_p/\partial t = 0$. In Eq. (23), only the component $\boldsymbol{\lambda}_r$ of the costate is discontinuous since $\partial S_p/\partial \boldsymbol{r} \neq \boldsymbol{0}^\top$. Let π_t and π_ε be the scalar multipliers for the time- and energy-to-fuel-optimal problems, respectively. The following can be said:

Energy-to-fuel-optimal problem The Hamiltonian function at t_s^- and t_s^+ is

$$H_\varepsilon(t_s^-) = \boldsymbol{\lambda}_r(t_s^-) \cdot \boldsymbol{v} - \frac{\mu}{r^3}\boldsymbol{\lambda}_v \cdot \boldsymbol{r} + u(t_s^-)\frac{T_{\max}}{I_{\text{sp}}\, g_0}(S_\varepsilon - \varepsilon + \varepsilon u(t_s^-)) \tag{24}$$

$$H_\varepsilon(t_s^+) = \boldsymbol{\lambda}_r(t_s^+) \cdot \boldsymbol{v} - \frac{\mu}{r^3}\boldsymbol{\lambda}_v \cdot \boldsymbol{r} + u(t_s^+)\frac{T_{\max}}{I_{\text{sp}}\, g_0}(S_\varepsilon - \varepsilon + \varepsilon u(t_s^+)) \tag{25}$$

Combining Eq. (22), (24), and (25) yields

$$\pi_\varepsilon = \Delta u \frac{T_{\max}}{I_{\text{sp}}\, g_0} \frac{S_\varepsilon - \varepsilon + (u(t_s^+) + u(t_s^-))\varepsilon}{\dot{S}_p} \tag{26}$$

where $\Delta u = u(t_s^+) - u(t_s^-)$ and $\dot{S}_p = (\partial S_p/\partial \boldsymbol{r})\dot{\boldsymbol{r}}$.

Remark 3 *Let $\boldsymbol{y}(t) = \boldsymbol{\varphi}_\varepsilon(\boldsymbol{y}_i, t_i, t)$ be the solution flow for a specified ε value of Eq.* (14) *integrated from the initial time t_i to a generic time t, using $\boldsymbol{x}_i$, $\boldsymbol{\lambda}_i$ at t_i, $\boldsymbol{\alpha}^*$ in Eq.* (10) *and u^* in Eq.* (13). *$\boldsymbol{\lambda}_r(t_s^+)$ is computed through Eq.* (23) *if S_p*

crosses $P_{\min}$ at t_s. The energy-to-fuel optimal problem is to find $\boldsymbol{\lambda}_i^*$ such that $\boldsymbol{y}(t_f) = \boldsymbol{\varphi}_\varepsilon([\boldsymbol{x}_i, \boldsymbol{\lambda}_i^*], t_i, t_f)$ satisfies Eqs. (7) and (15).

Time-optimal problem The Hamiltonian function at t_s^- and t_s^+ is

$$H_t(t_s^-) = \boldsymbol{\lambda}_r(t_s^-) \cdot \boldsymbol{v} - \frac{\mu}{r^3}\boldsymbol{\lambda}_v \cdot \boldsymbol{r} + u(t_s^-)\frac{T_{\max}}{I_{\text{sp}}\, g_0} S_t + 1 \tag{27}$$

$$H_t(t_s^+) = \boldsymbol{\lambda}_r(t_s^+) \cdot \boldsymbol{v} - \frac{\mu}{r^3}\boldsymbol{\lambda}_v \cdot \boldsymbol{r} + u(t_s^+)\frac{T_{\max}}{I_{\text{sp}}\, g_0} S_t + 1 \tag{28}$$

Combining Eqs. (22), (27), and (28) yields

$$\pi_t = \Delta u \frac{T_{\max}}{I_{\text{sp}}\, g_0} \frac{S_t}{\dot{S}_p} \tag{29}$$

Remark 4 *Let $\boldsymbol{y}(t) = \boldsymbol{\varphi}_t(\boldsymbol{y}_i, t_i, t)$ be the solution flow of Eq. (21) integrated from initial time t_i to a generic time t, using $\boldsymbol{x}_i$, $\boldsymbol{\lambda}_i$ at t_i, $\boldsymbol{\alpha}^*$ in Eq. (10) and u^* in Eq. (18). $\boldsymbol{\lambda}_r(t_s^+)$ is computed through Eq. (23) if S_p crosses $P_{\min}$ at t_s. The time-optimal problem is to find $\boldsymbol{\lambda}_i^*$ and t_f^* such that $\boldsymbol{y}(t_f) = \boldsymbol{\varphi}_t([\boldsymbol{x}_i, \boldsymbol{\lambda}_i^*], t_i, t_f^*)$ satisfies Eqs. (7), (15) and (20).*

Remark 5 *It is assumed that singular arcs where $S_t = 0$ in the time-optimal problem and $S_\varepsilon = 0$ in the fuel-optimal problem are absent over finite time intervals. Also, it is assumed that S_p crosses $P_{\min}$ isolated with $\dot{S}_p \neq 0$.*

Remark 6 *A NOCP with interior-point constraints is inherently a MPBVP [5]. By leveraging the analytical expressions of π_ε in Eq. (26) and π_t in Eq. (29), this MPBVP is transformed into a TPBVP as stated in Remarks 3 and 4.*

III. Initialization of Guess Solution

The Adjoint Control Transformation (ACT) [16] is used to guess initial costates of time- and energy-optimal problems. The idea is to map the estimation of physical control variables and their derivatives to initial costates at t_i, i.e., $\mathcal{M} : (\alpha_i, \dot{\alpha}_i, \beta_i, \dot{\beta}_i, S_i, \dot{S}_i) \to (\boldsymbol{\lambda}_{ri}, \boldsymbol{\lambda}_{vi})$, where α_i and β_i are the in-plane and out-of-plane thrust angles in a spacecraft-centered frame [16], S_i and $\dot{S}_i$ are initial values of the switching function and its derivative. However, as shown in Eqs. (13) and (18), power constraints may cause discontinuities in u for time- and energy-optimal problems, which deteriorates the performance of ACT. In these cases, the Hyperbolic Tangent Smoothing (HTS) method in [17] is used. The idea is to replace $T_{\max}$ in the above equations with $\tilde{T}_{\max}$ defined as

$$\tilde{T}_{\max} \coloneqq \begin{cases} T_{\max} \times \hbar(\rho, \boldsymbol{r}) = T_{\max} \times \dfrac{1}{2}\left[\tanh\left(\dfrac{P_{\text{in}} - P_{\min}}{\rho/\text{PU}}\right) + 1\right] & \rho > 0 \\ T_{\max} & \rho = 0 \end{cases} \tag{30}$$

where ρ is a smoothing factor and PU is the power unit.

Starting from $\rho = \rho_0 > 0$ (a manually selected value), $\tilde{T}_{\max}$ approaches $T_{\max}$ while gradually reducing $\rho \to 0$. Here, ACT is used to guess the initial costate to the problem with ρ_0. The improvement to the HTS method in [17] is that the proposed method allows reaching $\rho = 0$, which corresponds to the desired discontinuous solution. This feature is desirable to better assess the HTS method and better understand the optimal solution. Since the power unit PU used in the simulations (see Table 1 in Sec. VI) is large compared to P_{in}, PU is inserted in Eq. (30) to ease the selection of ρ_0.

The approximate Hamiltonian functions when using Eq. (30) are given by replacing $T_{\max}$ in Eqs. (9) and (17) with $\tilde{T}_{\max}$. The switching functions (Eqs. (12) and (19)) and the optimal control policies (Eqs. (13) and (18)) remain unaltered because they are independent on $T_{\max}$. Since discontinuous control is approximated by continuous control, the interior-point constraints are not triggered. Thus, the HTS approaches the solution to the MPBVP by solving a consecutive sequence of TPBVPs. The dynamics for the approximate time- and energy-to-fuel-optimal problems are simply given by replacing $T_{\max}$ in Eqs. (14) and (21) with $\tilde{T}_{\max}$.

IV. Analytic Derivatives

The variational method exploits the state transition matrix (STM) and the chain rule to compute the gradients [16]. The STM maps small variations in the initial conditions $\delta \boldsymbol{y}_i$ over $t_i \to t$, i.e., $\delta \boldsymbol{y}(t) = \Phi(t_i, t)\delta \boldsymbol{y}(t_i)$. The STM is subject to the variational equation

$$\dot{\Phi}(t_i, t) = D_y \boldsymbol{F}\ \Phi(t_i, t), \quad \Phi(t_i, t_i) = \boldsymbol{I}_{14\times 14} \tag{31}$$

where $D_{\boldsymbol{y}} \boldsymbol{F}$, the Jacobian matrix of $\boldsymbol{F}(\boldsymbol{y})$, has two different expressions based on whether u^* is constant or not. Let $z := [\boldsymbol{y}^\top, \text{vec}(\Phi)^\top]^\top$ be a 210-dimensional vector containing $\boldsymbol{y}$ and the columns of Φ, where 'vec' is the operator that converts a matrix into a column vector. There exists

$$\dot{z} = \boldsymbol{G}(z) \Rightarrow \begin{pmatrix} \dot{\boldsymbol{y}} \\ \text{vec}(\dot{\Phi}) \end{pmatrix} = \begin{pmatrix} \boldsymbol{F}(\boldsymbol{y}) \\ \text{vec}(D_{\boldsymbol{y}} \boldsymbol{F}\ \Phi) \end{pmatrix} \tag{32}$$

Note that Φ maps states and costates along a continuous orbit. When a discontinuity is encountered at the switching time t_s, the STM compensation $\Psi(t_s)$ across the discontinuity should be determined [16]. Suppose there are N discontinuities at $t_1, t_2, \cdots, t_N$, the STM is calculated using the chain rule as

$$\Phi(t_f, t_i) = \Phi(t_f, t_N^+)\Psi(t_N)\Phi(t_N^-, t_{N-1}^+)\Psi(t_{N-1})\cdots\Phi(t_2^-, t_1^+)\Psi(t_1)\Phi(t_1^-, t_i) \tag{33}$$

Suppose that the discontinuity detected at t_s is indicated by a switching function S crossing a threshold η, then there are three possible cases:

- Case 1: $S = S_\varepsilon$, $\varepsilon = 0$, $\eta = 0$; u jumps between 0 and 1 at t_s.

- Case 2: $S = S_p$, $u \neq 0$, $\eta = P_{\min}$; u jumps between a non-zero value and 0 at t_s.
- Case 3: $S = S_p$, $\eta = P_{\max}$; u remains the same, but the costate dynamics are discontinuous at t_s.

Based on the method in [16], analytical expressions of $\Psi(t_s)$ are obtained. Cases 1 and 3 belong to the first category, where $\boldsymbol{y}$ is continuous but $\dot{\boldsymbol{y}}$ is discontinuous. $\Psi(t_s)$ satisfies

$$\Psi(t_s) = \frac{\partial \boldsymbol{y}(t_s^+)}{\partial \boldsymbol{y}(t_s^-)} = I_{14\times 14} + \left(\dot{\boldsymbol{y}}(t_s^+) - \dot{\boldsymbol{y}}(t_s^-)\right) \frac{1}{\dot{S}} \frac{\partial S}{\partial \boldsymbol{y}} \tag{34}$$

Case 2 belongs to the second category, where both $\boldsymbol{y}$ and $\dot{\boldsymbol{y}}$ are discontinuous. $\Psi(t_s)$ satisfies

$$\Psi(t_s) = \frac{\partial \boldsymbol{y}(t_s^+)}{\partial \boldsymbol{y}(t_s^-)} = I_{14\times 14} + \frac{\partial \Delta \boldsymbol{y}}{\partial \boldsymbol{y}} + \left(\dot{\boldsymbol{y}}(t_s^+) - \dot{\boldsymbol{y}}(t_s^-) - \Delta \dot{\boldsymbol{y}}\right) \frac{1}{\dot{S}_p} \frac{\partial S_p}{\partial \boldsymbol{y}} \tag{35}$$

where $\Delta \dot{\boldsymbol{y}} = \dfrac{\partial \Delta \boldsymbol{y}}{\partial \boldsymbol{y}} \dot{\boldsymbol{y}}(t_s^-)$.

Remark 7 *When the input power reaches its upper and lower bounds, the gradients are compensated through Eqs.* (34) *and* (35)*, respectively.*

V. Switching Detection Technique

The detection of the switching time t_s is essential for the STM and solution accuracy. Consider a switching function S and the constant threshold η, the task is to find t_s such that $S(\boldsymbol{y}(t_s)) = \eta$. Suppose that at consecutive times t_k and t_{k+1}, there exists $(S(\boldsymbol{y}_k) - \eta) \times (S(\boldsymbol{y}_{k+1}) - \eta) < 0$, where $\boldsymbol{y}_k := \boldsymbol{y}(t_k)$ and $\boldsymbol{y}_{k+1} := \boldsymbol{y}(t_{k+1})$. Then the switching time determination algorithm depicted in [18] is used to search $t_s \in [t_k, t_{k+1}]$, with 10^{-12} tolerance.

The low-thrust trajectory optimization problem has been implemented in a numerical framework. To ease the discussion, let p_{type} and u_{type} be the status of the available power input and the thrust throttle, respectively. When $\rho = 0$, the logic is

$$p_{\text{type}} = \begin{cases} \text{On}, & \text{if} \quad S_p \geq P_{\max} \\ \text{Medium}, & \text{if} \quad S_p \in [P_{\min}, P_{\max}) \\ \text{Off}, & \text{if} \quad S_p < P_{\min} \end{cases}, \quad u_{\text{type}} = \begin{cases} \text{On}, & \text{if} \quad u = 1 \\ \text{Medium}, & \text{if} \quad u \in (0,1) \\ \text{Off}, & \text{if} \quad u = 0 \end{cases} \tag{36}$$

When $\rho \neq 0$, u_{type} is the same as in Eq. (36), but p_{type} becomes

$$p_{\text{type}} = \begin{cases} \text{On}, & \text{if} \quad S_p \geq P_{\max} \\ \text{Medium}, & \text{if} \quad S_p < P_{\max} \end{cases} \tag{37}$$

thus $p_{\text{type}} = \text{Off}$ is not used for $\rho \neq 0$.

The presented integration flowchart in Fig. 2 augments the flowchart in [18] (shown with dashed blocks) in order to effectively tackle power constraints. The inputs required to execute an integration step are 1) t_k, the k–th integration time; 2) h_p, the step size predicted by previous integration step; 3) z_k, the 210-dimensional state at t_k; 4) u_{type}, the logical type of the thrust throttle; 5) p_{type}, the logical type of the power input; 6) ρ, the smoothing factor. Three branches emanate according to u_{type}, and for each integration block, a prediction on z_{k+1}, e.g., $z_{k+1} = \boldsymbol{\psi}_{\text{RK}}(z_k, t_k, t_k + h_p, u_{\text{type}}, p_{\text{type}}, \rho)$, is executed, using a variable-step seventh/eighth Runge–Kutta integration scheme. Note that z_{k+1} is the state corresponding to $t_{k+1} = t_k + h_f$, where h_f is the corrected time step during Runge–Kutta integration [18]. For the time-optimal problem, $\varepsilon = 0$ in Fig. 2.

For u_{type} being On or Medium and $\rho = 0$, the execution blocks are similar. The branch u_{type} = On is analyzed below without losing generality. Since the engine is enforced to switch off in case of insufficient power P_{in}, the fist task after one-step integration prediction is to check the power status $p_{\text{type},k+1}$ corresponding to z_{k+1}. If $p_{\text{type},k+1}$ = Off, indicating that S_p crosses P_{min}, it is then required to execute Block 2 where the power switching time t_s is detected. Let z_s be the 210-dimensional vector, and S_c be the value of S_ε (energy-to-fuel-optimal problem) or S_t (time-optimal problem) at t_s. If $S_c < -\varepsilon$, the STM is computed using Eq. (35) which is then stored in z_s. z_{k+1} and t_{k+1} used for the next integration step are saved as $z_{k+1} = z_s$ and $t_{k+1} = t_s$. u_{type} is updated to Off and p_{type} is updated to $p_{\text{type},k+1}$. Otherwise if $S_c > -\varepsilon$, indicating that the throttle switching arises within $[t_k, t_{k+1}]$, thus h_p is reduced.

If $p_{\text{type},k+1} \neq$ Off, the comparison of p_{type} and $p_{\text{type},k+1}$ is made. If $p_{\text{type}} \neq p_{\text{type},k+1}$, indicating that S_p crosses P_{max}, then Block 2 is executed. If $S_c < -\varepsilon$ is further satisfied, the STM is computed using Eq. (34). z_{k+1} and t_{k+1} are saved as $z_{k+1} = z_s$ and $t_{k+1} = t_s$. p_{type} is updated to $p_{\text{type},k+1}$. Otherwise, if $p_{\text{type}} = p_{\text{type},k+1}$, the thrust throttle is determined by S_{k+1} that is the value of S_ε (energy-to-fuel-optimal problem) or S_t (time-optimal problem) at t_{k+1}, and the branch u_{type} = On of the flowchart in [18] is executed. For the case $\rho \neq 0$, the implementation is the same except that the branch $p_{\text{type},k+1}$ = Off is not executed.

For u_{type} being Off, the first task after the one-step integration prediction is to verify the reason that conduces the engine to switch off. If p_{type} = Off, then $u = 0$ is caused by insufficient input power. In this case, if $p_{\text{type},k+1}$ = Off, the solution is saved. Otherwise if $p_{\text{type},k+1} \neq$ Off, indicating that sufficient power is available for the next step, then Block 2 is executed. The $u(t_s^+)$ after t_s is determined by S_c. For example, if $S_c < -\varepsilon$, then the STM is calculated using Eq. (35). z_{k+1} and t_{k+1} are saved as $z_{k+1} = z_s$ and $t_{k+1} = t_s$. u_{type} is updated to On. p_{type} is updated to $p_{\text{type},k+1}$.

If $p_{\text{type}} \neq$ Off, meaning that the engine switches off due to $S_k > \varepsilon$. If $p_{\text{type},k+1}$ = Off, Block 2 is executed. Since no discontinuity exists, it is not necessary to update the STM, but the power status is updated if $S_c > \varepsilon$. Otherwise if $p_{\text{type},k+1} \neq$ Off, the check whether $p_{\text{type},k}$ equals to $p_{\text{type},k+1}$ is executed. If $p_{\text{type}} \neq p_{\text{type},k+1}$, implying that S_p crosses P_{max}, Block 2 is executed. The power status is updated if $S_c > \varepsilon$. If $p_{\text{type}} = p_{\text{type},k+1}$, the branch u_{type} = Off of the flowchart in [18] is executed.

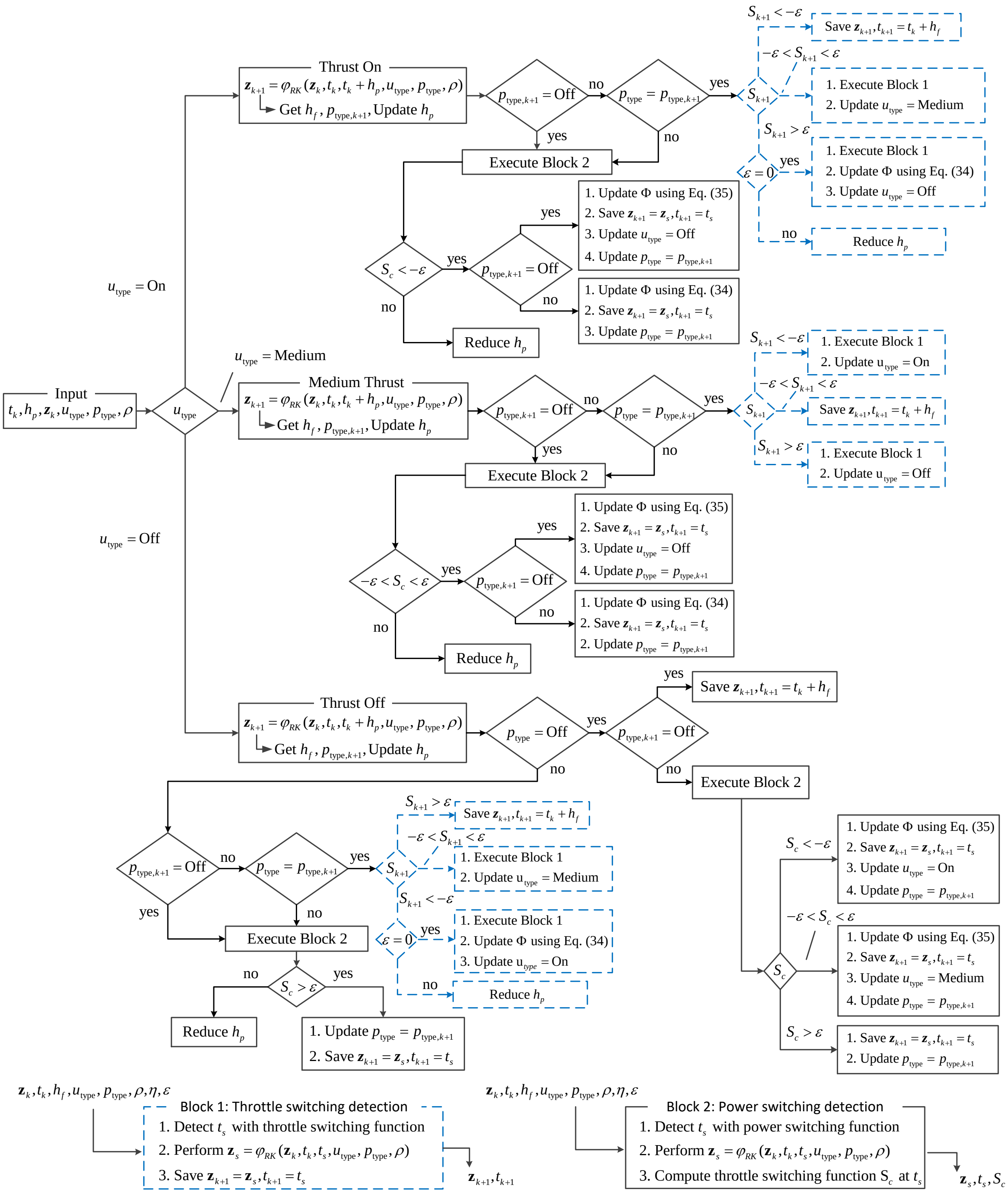

Fig. 2 Flowchart for the implementation of a generic integration step. Dashed blocks are from [18].

VI. Numerical Simulations

The M-ARGO Cubesat mission to the near-Earth asteroid 2000 SG344 is simulated [20]. The physical constants are listed in Table 1. The thruster model is handled using fourth-order polynomials as in [20]

$$\begin{aligned} T_{\max}(P_{\text{in}}) &= a_0 + a_1 P_{\text{in}} + a_2 P_{\text{in}}^2 + a_3 P_{\text{in}}^3 + a_4 P_{\text{in}}^4 \\ I_{\text{sp}}(P_{\text{in}}) &= b_0 + b_1 P_{\text{in}} + b_2 P_{\text{in}}^2 + b_3 P_{\text{in}}^3 + b_4 P_{\text{in}}^4 \\ S_p(r) &= c_0 + c_1 r + c_2 r^2 + c_3 r^3 + c_4 r^4 \end{aligned}$$

where the coefficients are listed in Table 2. Figure 3 illustrates the variations of P_{in}, $T_{\max}$ and I_{sp} w.r.t. the scaled Sun-spacecraft distance r, with $P_{\max} = 120$ W. It can be seen that at 1 AU we have $P_{\text{in}} = 105.4$ W, $T_{\max} = 1.89$ mN and $I_{\text{sp}} = 3022.59$ s. The comparison between the $1/r^2$ law, S_p and P_{in} is also shown in Fig. 3a, where P_{in} reaches $P_{\max}$ when $r \leq 0.928$ AU.

Table 1 Physical constants.

Physical constant	Value
Mass parameter, μ	1.327124×10^{11} km^3/s^2
Gravitational field, g_0	9.80665 m/s^2
Astronomical unit, AU	1.495979×10^8 km
Time unit, TU	5.022643×10^6 s
Velocity unit, VU	29.784692 km/s
Mass unit, MU	22.6 kg
Power unit, PU	3991.74 W

Table 2 Thruster coefficients.

$T_{\max}$	Value	Unit	I_{sp}	Value	Unit	S_p	Value	Unit
a_0	−0.7253	mN	b_0	2652	s	c_0	840.11	W
a_1	0.02481	mN/W	b_1	−18.123	s/W	c_1	−1754.3	W/AU
a_2	0		b_2	0.3887	s/W^2	c_2	1625.01	W/AU^2
a_3	0		b_3	−0.00174	s/W^3	c_3	−739.87	W/AU^3
a_4	0		b_4	0		c_4	134.45	W/AU^4

The asteroid ephemerides are given by SPICE kernel from HORIZONS system [23] *. As a study case, the launch time is set to 1st Jan 2022, whereas the arrival date is set to 1st Jun 2024 for the energy- and fuel-optimal problems. The initial mass is set to 22.6 kg, the same as MU in Table 1. The spacecraft is supposed to depart from Sun–Earth L_2 Lagrange point, and corresponding boundary conditions provided by HORIZON system are shown in Table 3, where

*See https://ssd.jpl.nasa.gov/?horizons

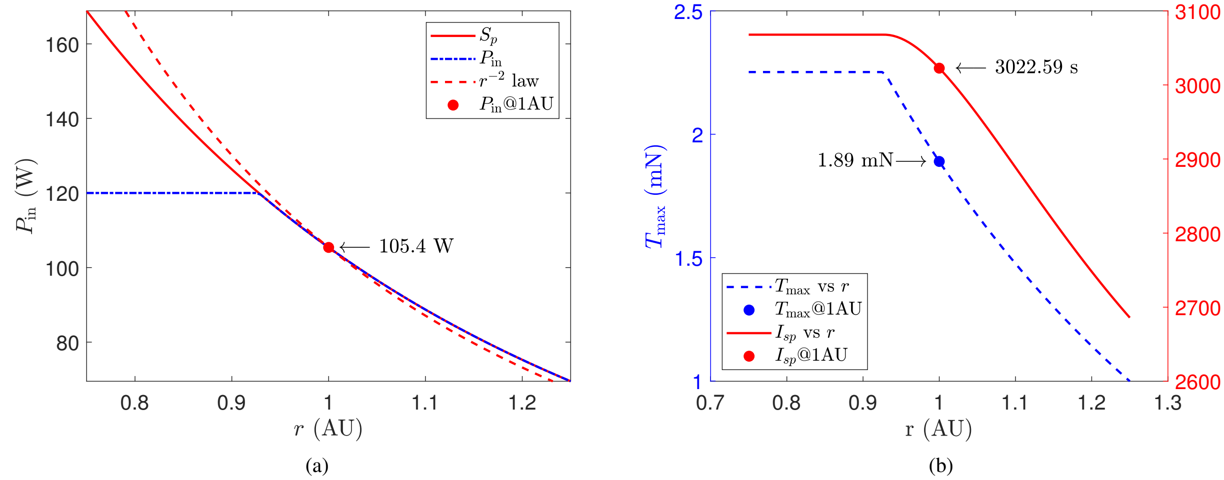

Fig. 3 Variation of $P_{\rm in}$, $T_{\max}$ and $I_{\rm sp}$ w.r.t. r with $P_{\max} = 120$ W.

terminal position and velocity conditions are used for the energy- and fuel-optimal problems in Sec. VI.B. Terminal position and velocity conditions for the time-optimal problem in Sec. VI.A depend on guessed transfer time and are varied during the optimization. All simulations are conducted under an Intel Core i7–9750H, CPU@2.6GHz, Windows 10 system with MATLAB R2019a. The integration code is converted to MEX file to speed up simulations.

A total of 6 cases in Table 4 are simulated. The inputs $(\alpha_i, \dot{\alpha}_i, \beta_i, \dot{\beta}_i, S_i, \dot{S}_i)$ of ACT are randomly generated at the initial time within given bounds. The shape-based method in [24] has been employed for case 5 to provide an intuition of initial thrust angles. It shows that the thrust direction at the initial time is close to the velocity. Thus the bounds are set up as follows: $\alpha_i \in [-10, 10]$ deg, $\dot{\alpha}_i \in [-5, 5]$ deg/TU, $\beta_i \in [-1, 1]$ deg and $\dot{\beta}_i \in [-0.1, 0.1]$ deg/TU. The initial mass costate is set to 1. From Eq. (12) and (19), S_i has to be negative. The bounds of S_i and $\dot{S}_i$ are: $S_i \in [-1.5, -0.001]$ and $\dot{S}_i \in [-0.01, 0.01]$.

Table 3 Boundary Conditions.

Boundary Condition	Value
Initial position vector, AU	$[-0.1764352209, 0.9774432047, -4.6698040914 \times 10^{-5}]^\top$
Initial velocity vector, VU	$[-1.0105715460, -0.1832792298, 1.2539059040 \times 10^{-5}]^\top$
Terminal position vector, AU	$[-0.6547598563, 0.6446483464, -1.5061497361 \times 10^{-3}]^\top$
Terminal velocity vector, VU	$[-0.7759381160, -0.7425308483, 1.1204008105 \times 10^{-3}]^\top$

A. Time-Optimal Transfers

Two time-optimal problems for $P_{\min} = 0$ W and $P_{\min} = 95$ W are solved for comparison. The transfer time is monotonically increased (starting from 1 year) until the solution is found. For each guessed t_f, the ACT map is executed

Table 4 Simulation results.

Case	Type	$P_{\min}$, W	Optimal costate vector $\boldsymbol{\lambda}_i^*$	t_f^*, days	m_f, kg
1	TO[a]	0	$[15.42735, -61.81391, 0.18480, 74.40205, 4.50555, 0.04902, 4.38101]^\top$	593.2311	19.7994
2	TO	95	$[-11.00728, -175.41465, 1.40145, 155.51247, 57.39753, 0.24116, 7.10106]^\top$	699.0125	20.6825
3	EO[b]	0	$[0.32576, -0.97280, 0.03702, 1.20654, 0.00762, 0.00254, 0.05948]^\top$	821	21.1738
4	EO	95	$[0.31165, -2.07603, 0.06691, 2.45955, 0.32964, 0.00996, 0.14322]^\top$	821	20.8288
5	FO[c]	0	$[0.31717, -0.97395, 0.22169, 1.19851, 0.01910, 0.01280, 0.05682]^\top$	821	21.4370
6	FO	95	$[0.23645, -1.28756, 0.08292, 1.61084, 0.17194, 0.04682, 0.11054]^\top$	821	20.9239

[a] time-optimal solution; [b] energy-optimal solution; [c] fuel-optimal solution;

5 times at most. The corresponding solutions are summarized as cases 1–2 in Table 4. For case 1, since $S_p < P_{\min}$ is not triggered, the HTS is not used. The time-optimal trajectory is shown in Fig. 4a. The variations of u, S_t, m, P_{in}, I_{sp} and $T_{\max}$ are shown in Fig. 4b, where the engine is always 'on'. The minimum transfer time is 593.2311 days and the final mass of the spacecraft is 19.7994 kg.

For case 2, the HTS is used first to find the approximate solution corresponding to $\rho_0 = 4$, then ρ is gradually reduced to approach the optimal solution ($\rho_0 = 0$). The corresponding time-optimal trajectory is shown in Fig. 5a, and the variations of u, S_t, m, P_{in}, I_{sp} and $T_{\max}$ are shown in Fig. 5b. The minimum transfer time 699.0125 days, and the final mass of the spacecraft is 20.6825 kg. Compared to case 1, the engine switches off twice due to insufficient input power, after 95.57 and 552.54 days of flight. The engine-off lasts for 273.02 and 58.69 days, respectively. The transfer time is 105.78 days longer than that of case 1, whereas 0.8831 kg of fuel is saved. Figure 6 shows the variations of $\boldsymbol{\lambda}_r$, where $\boldsymbol{\lambda}_r$ is discontinuous when P_{in} crosses $P_{\min}$ and $\Delta u \neq 0$.

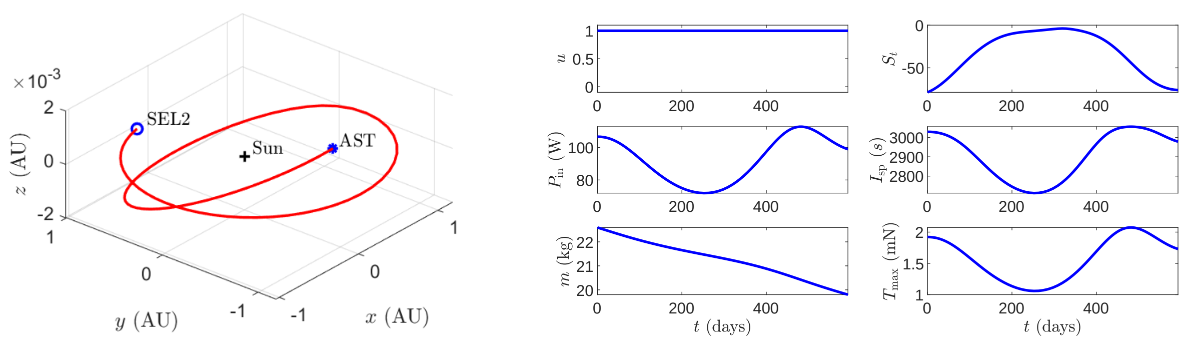

(a) Time-optimal trajectory.

(b) Variations of u, P_{in}, m, S_t, I_{sp} and $T_{\max}$.

Fig. 4 Case 1: time-optimal solution. SEL2: Sun–Earth L_2 Lagrange point; AST: asteroid position at arrival.

B. Fuel-Optimal Transfers

Fuel-optimal transfers for $P_{\min} = 0\ W$ and $P_{\min} = 95\ W$ are solved. The energy-optimal (cases 3 and 4) and fuel-optimal (cases 5 and 6) solutions are shown in Table 4, respectively. For cases 3-4, the HTS is not used. The

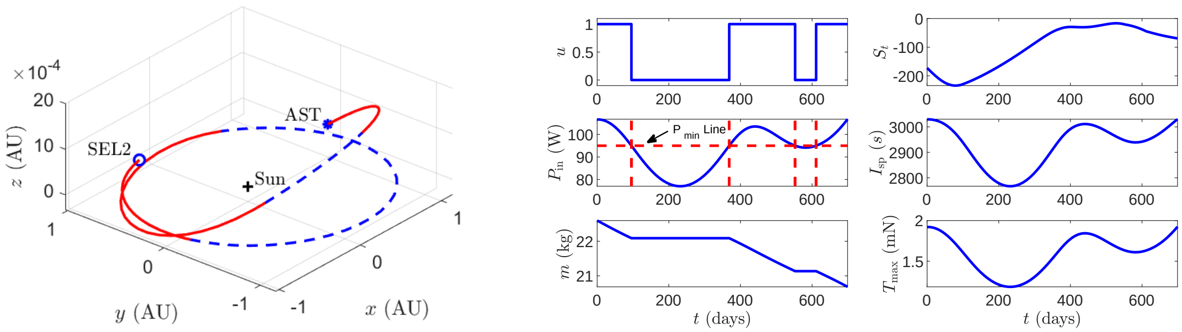

(a) Time-optimal trajectory.

(b) Variations of u, P_{in}, m, S_t, I_{sp} and $u\,T_{\max}$.

Fig. 5 Case 2: time-optimal solution. SEL2: Sun–Earth L_2 Lagrange point; AST: asteroid position at arrival.

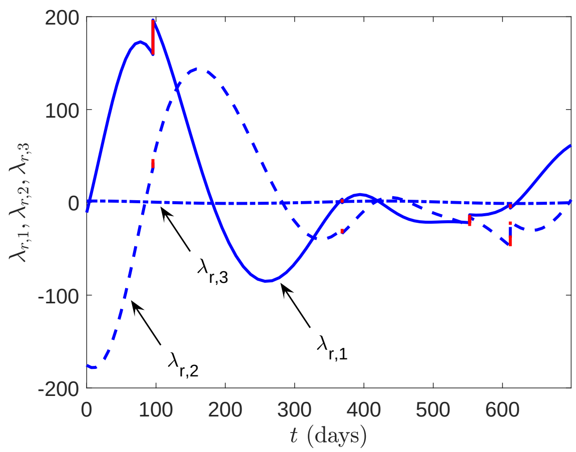

Fig. 6 Variations of optimal λ_r w.r.t. time for case 2. The discontinuities of λ_r are labeled red.

corresponding fuel-optimal trajectory is shown in Fig. 7a. The variations of u, S_f, m, P_{in}, I_{sp} and $T_{\max}$ are shown in Fig. 7b, where $P_{\max}$ is reached after around 767.60 days of flight. The final mass of the spacecraft is 21.4370 kg.

For cases 5-6, the HTS is used to solve the approximate energy-optimal problem first, with $\rho_0 = 4$. The energy-optimal solution is found by gradually reducing ρ to 0. Then, the fuel-optimal solution is gradually approached by reducing ε to 0, with $\Delta\varepsilon = 0.05$ steps. The step is halved if the continuation fails. The corresponding fuel-optimal trajectory is shown in Fig. 8a. The variations of u, S_f and m, P_{in}, I_{sp} and $T_{\max}$ are shown in Fig. 8b. The variations of $\boldsymbol{\lambda}_r$ is shown in Fig. 9. The final mass of the spacecraft is 20.9239 kg. The insufficient input power is encountered twice, after 92.16 and 532.08 days of flight, and the engine-off lasts for 262.26 and 107.69 days, respectively. The maximum input power is encountered after 764.47 days of flight until to the end. Compared to the fuel-optimal solution of case 5, case 6 requires 0.5131 kg more fuel. In terms of computational time, the HTS and energy- to fuel-optimal continuation (not involving ACT) in case 6 takes around 4 s, while it takes around 27 s if the gradients are computed by finite differences. The benefits of the variational method become tremendous in terms of computational time especially when a multitude of trajectories are required [20].

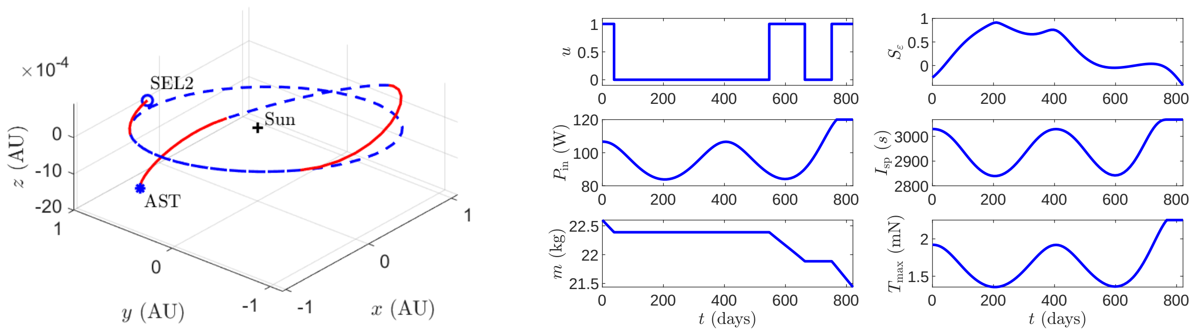

(a) Fuel-optimal trajectory.

(b) Variations of u, P_{in}, m, S_ε, $u\,T_{\max}$ and I_{sp}.

Fig. 7 Case 5: fuel-optimal solution. SEL2: Sun–Earth L_2 Lagrange point; AST: asteroid position at arrival.

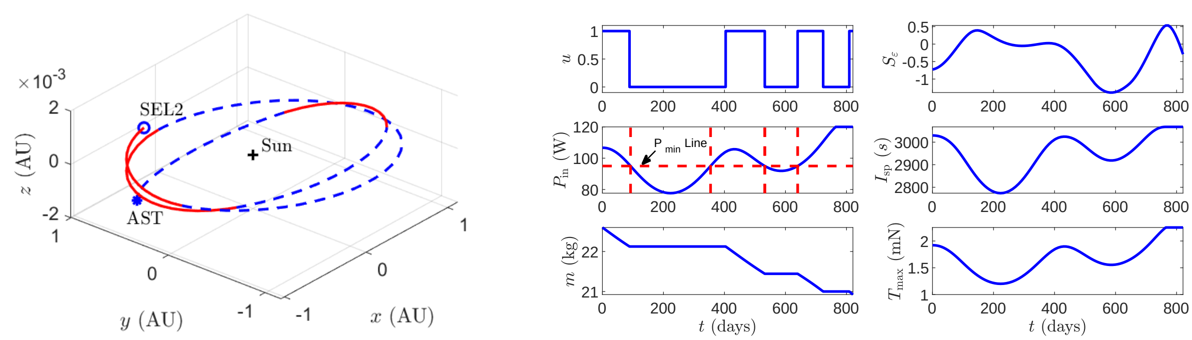

(a) Fuel-optimal trajectory.

(b) Variations of u, P_{in}, m, S_ε, $T_{\max}$ and I_{sp}.

Fig. 8 Case 6: fuel-optimal solution. SEL2: Sun–Earth L_2 Lagrange point; AST: asteroid position at arrival.

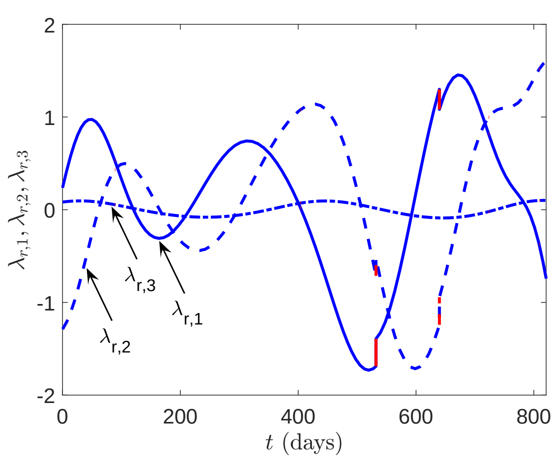

Fig. 9 Variations of optimal λ_r w.r.t. time for case 6. The discontinuities of λ_r labeled red.

C. Discussion

A comparison of thrust profiles for both time-optimal and fuel-optimal problems using GPOPS [25] is performed (Fig. 10). It is clear that GPOPS solutions coincide with solutions obtained by using the proposed method. Note that GPOPS handles cases 1 and 5 as single phase problems, while it solves cases 2 and 6 as multi-phase problems, since these are inherently MPBVPs. When the desired discontinuous solution is required, the presented method has the advantage of solving the MPBVP as a TPBVP. Thus HTS can be embedded into the computational framework. Also, there is no need to specify the solution structure a priori. On the other hand, GPOPS has to solve the MPBVP separately with HTS, and the solution structure must be guessed beforehand.

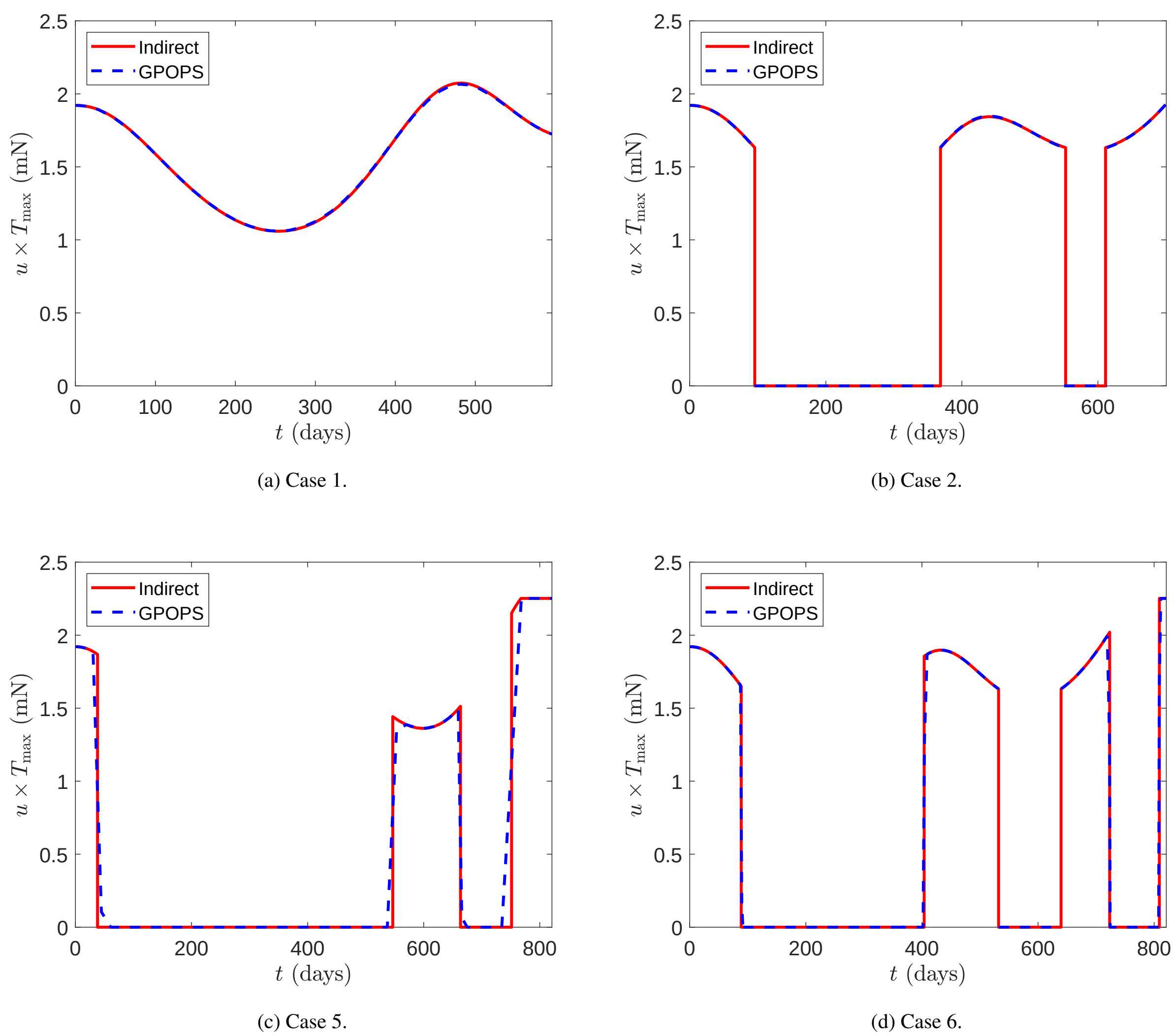

(a) Case 1. (b) Case 2. (c) Case 5. (d) Case 6.

Fig. 10 Comparisons of time-optimal and fuel-optimal $u \times T_{\max}$ profiles to GPOPS solutions.

VII. Conclusions

The effects of thruster power constraints on indirect optimization are investigated. The gradients at discrete, discontinuous points produced by power constraints are investigated by analyzing the behavior of the state transition matrix. The problem becomes complicated when the input power reaches its lower bound, and costates become discontinous. By leveraging the analytical multipliers related to the scalar interior-point constraints, an efficient indirect method has been developed, which allows for solving a MPBVP as a TPBVP. The computational framework for solving both time- and fuel-optimal problems is established by combining analytic derivatives, continuation, and switching detection into an augmented flowchart. The outcome is an algorithm that features accurate bang-bang solutions and gradients with broader convergence domain and high computational efficiency. Thus, the presented method is useful when solving a multitude of problems in the context of asteroid target screening [20]. Moreover, the proposed method is useful for solving bang-bang control problems with scalar interior-point constraints, such as the Earth-orbit low-thrust transfer problem with shadow constraints [26].

Acknowledgment

Part of this work has been funded by ESA through contract No. 4000127373/19/NL/AF (M-ARGO mission Phase A study).

Conflict of Interest Statement

We have no conflict of interest to declare.

References

[1] Quadrelli, M., Wood, L., Riedel, J., McHenry, M., Aung, M., Cangahuala, L., Volpe, R., Beauchamp, P., and Cutts, J., "Guidance, Navigation, and Control Technology Assessment for Future Planetary Science Missions," *Journal of Guidance, Control, and Dynamics*, Vol. 38, No. 7, 2015, pp. 1165–1186. doi:10.2514/1.G000525.

[2] Betts, J., "Survey of Numerical Methods for Trajectory Optimization," *Journal of guidance, control, and dynamics*, Vol. 21, No. 2, 1998, pp. 193–207. doi:10.2514/2.4231.

[3] Conway, B., "A Survey of Methods Available for the Numerical Optimization of Continuous Dynamic Systems," *Journal of Optimization Theory and Applications*, Vol. 152, No. 2, 2012, pp. 271–306. doi:10.1007/s10957-011-9918-z.

[4] Herman, A., and Conway, B., "Direct Optimization Using Collocation based on High-Order Gauss-Lobatto Quadrature Rules," *Journal of Guidance, Control, and Dynamics*, Vol. 19, No. 3, 1996, pp. 592–599. doi:10.2514/3.21662.

[5] Guo, T., Li, J., Baoyin, H., and Jiang, F., "Pseudospectral Methods for Trajectory Optimization with Interior Point Constraints: Verification and Applications," *IEEE Transactions on Aerospace and Electronic Systems*, Vol. 49, No. 3, 2013, pp. 2005–2017. doi:10.1109/TAES.2013.6558034.

[6] Williams, S., and Coverstone-Carroll, V., "Benefits of Solar Electric Propulsion for the Next Generation of Planetary Exploration Missions," *The Journal of the Astronautical Sciences*, Vol. 45, No. 2, 1997, pp. 143–159. doi:10.1007/BF03546373.

[7] Oh, D., "Evaluation of Solar Electric Propulsion Technologies for Discovery-Class Missions," *Journal of Spacecraft and Rockets*, Vol. 44, No. 2, 2007, pp. 399–411. doi:10.2514/1.21613.

[8] Woolley, R., and Olikara, Z., "Optimized Low-Thrust Missions from GTO to Mars," *2019 IEEE Aerospace Conference*, IEEE, 2019, pp. 1–10. doi:10.1109/AERO.2019.8741558.

[9] Quarta, A., and Mengali, G., "Minimum-Time Space Missions with Solar Electric Propulsion," *Aerospace Science and Technology*, Vol. 15, No. 5, 2011, pp. 381–392. doi:10.1016/j.ast.2010.09.003.

[10] Mengali, G., and Quarta, A., "Fuel-Optimal, Power-Limited Rendezvous with Variable Thruster Efficiency," *Journal of Guidance, Control, and Dynamics*, Vol. 28, No. 6, 2005, pp. 1194–1199. doi:10.2514/1.12480.

[11] Li, T., Wang, Z., and Zhang, Y., "Double-Homotopy Technique for Fuel Optimization of Power-Limited Interplanetary Trajectories," *Astrophysics and Space Science*, Vol. 364, No. 9, 2019, p. 144. doi:10.1007/s10509-019-3637-6.

[12] Arya, V., Taheri, E., and Junkins, J., "Low-Thrust Gravity-Assist Trajectory Design Using Optimal Multimode Propulsion Models," *Journal of Guidance, Control, and Dynamics*, 2021, pp. 1–15. doi:10.2514/1.G005750.

[13] Taheri, E., Junkins, J., Kolmanovsky, I., and Girard, A., "A Novel Approach for Optimal Trajectory Design with Multiple Operation Modes of Propulsion System, Part 1," *Acta Astronautica*, Vol. 172, 2020, pp. 151–165. doi:10.1016/j.actaastro.2020.02.042.

[14] Chi, Z., Li, H., Jiang, F., and Li, J., "Power-Limited Low-Thrust Trajectory Optimization with Operation Point Detection," *Astrophysics and Space Science*, Vol. 363, No. 6, 2018, p. 122. doi:10.1007/s10509-018-3344-8.

[15] Pellegrini, E., and Russell, R., "On the Computation and Accuracy of Trajectory State Transition Matrices," *Journal of Guidance, Control, and Dynamics*, Vol. 39, No. 11, 2016, pp. 2485–2499. doi:10.2514/1.G001920.

[16] Russell, R., "Primer Vector Theory Applied to Global Low-Thrust Trade Studies," *Journal of Guidance, Control, and Dynamics*, Vol. 30, No. 2, 2007, pp. 460–472. doi:10.2514/1.22984.

[17] Taheri, E., and Junkins, J., "Generic Smoothing for Optimal Bang-Off-Bang Spacecraft Maneuvers," *Journal of Guidance, Control, and Dynamics*, Vol. 41, No. 11, 2018, pp. 2470–2475. doi:10.2514/1.G003604.

[18] Zhang, C., Topputo, F., Bernelli-Zazzera, F., and Zhao, Y.-S., "Low-Thrust Minimum-Fuel Optimization in the Circular Restricted Three-Body Problem," *Journal of Guidance, Control, and Dynamics*, Vol. 38, No. 8, 2015, pp. 1501–1510. doi:10.2514/1.G001080.

[19] Walker, R., Koschny, D., Bramanti, C., Carnelli, I., et al., "Miniaturised Asteroid Remote Geophysical Observer (M-ARGO): a Stand-Alone Deep Space CubeSat System for Low-Cost Science and Exploration Missions," *iCubeSat Workshop, Cambridge*, 2017, pp. 1–20.

[20] Topputo, F., Wang, Y., Carmine, G., Franzese, V., Goldberg, H., Perez-Lissi, F., and Walker, R., "Envelop of Reachable Asteroids by M-ARGO CubeSat," *Advances in Space Research*, Vol. 67, No. 12, 2021, pp. 4193–4221. doi:10.1016/j.asr.2021.02.031.

[21] Bertrand, R., and Epenoy, R., "New Smoothing Techniques for Solving Bang-Bang Optimal Control Problems-Numerical Results and Statistical Interpretation," *Optimal Control Applications and Methods*, Vol. 23, No. 4, 2002, pp. 171–197. doi:10.1002/oca.709.

[22] Bryson, A., and Ho, Y.-C., *Applied Optimal Control: Optimization, Estimation and Control*, Taylor and Francis Group, 1975. doi:10.1109/TSMC.1979.4310229, pp. 90–125.

[23] Giorgini, J., and Yeomans, D., "On-Line System Provides Accurate Ephemeris and Related Data," *NASA TECH BRIEFS, NPO-20416*, Vol. 48, 1999.

[24] Taheri, E., and Abdelkhalik, O., "Initial Three-Dimensional Low-Thrust Trajectory Design," *Advances in Space Research*, Vol. 57, No. 3, 2016, pp. 889–903. doi:10.1016/j.asr.2015.11.034.

[25] Rao, A., Benson, D., Darby, C., Patterson, M., Francolin, C., Sanders, I., and Huntington, G., "Algorithm 902: GPOPS, A MATLAB Software for Solving Multiple-Phase Optimal Control Problems Using the Gauss Pseudospectral Method," *ACM Transactions on Mathematical Software*, Vol. 37, 2010, pp. 1–39. doi:10.1145/1731022.1731032.

[26] Wang, Y., and Topputo, F., "Indirect Optimization for Low-Thrust Transfers with Earth-Shadow Eclipses," *31st AAS/AIAA Space Flight Mechanics Meeting*, Virtual, 2021. AAS 21-368.